
This manuscript is a preprint and has been submitted for publication in **Journal of Glaciology**. It has been revised after peer review but **not yet accepted for publication**. Subsequent versions of this manuscript may differ due to the editorial process. If accepted for publication, the final version will be available via the "Peer-reviewed publication DOI" link on EarthArXiv. We hope you find this paper interesting and would welcome your feedback on it. Please contact Mike Prior-Jones or Liz Bagshaw with your feedback using the email addresses on the following page.

1 Cryoegg: development and field trials of a wireless subglacial probe for deep, fast-moving ice

2 Michael Prior-Jones¹, Elizabeth A. Bagshaw¹, Jonathan Lees², Lindsay Clare³, Stephen Burrow³, Mauro
3 A Werder⁴, Nanna B. Karlsson⁵, Dorte Dahl-Jensen^{6,7}, Thomas R. Chudley⁸, Poul Christoffersen⁸,
4 Jemma Wadham⁹, Samuel H Doyle¹⁰, Bryn Hubbard¹⁰

5 ¹School of Earth and Ocean Sciences, Cardiff University, Cardiff, UK (prior-jonesm@cardiff.ac.uk;
6 bagshawe@cardiff.ac.uk)

7 ²School of Engineering, Cardiff University, Cardiff, UK

8 ³Department of Aerospace Engineering, University of Bristol, Bristol, UK

9 ⁴Laboratory of Hydraulics, Hydrology and Glaciology, ETH Zürich, Zürich, Switzerland

10 ⁵Geological Survey of Denmark and Greenland, Copenhagen, Denmark

11 ⁶Niels Bohr Institute, University of Copenhagen, Copenhagen, Denmark

12 ⁷Center for Earth Observation Science, University of Manitoba, Winnipeg, Canada

13 ⁸Scott Polar Research Institute, University of Cambridge, Cambridge, UK

14 ⁹School of Geographical Sciences, University of Bristol, Bristol, UK

15 ¹⁰Department of Geography and Earth Sciences, Aberystwyth University, Aberystwyth, UK

16 ABSTRACT

17 Subglacial hydrological systems require innovative technological solutions to access and observe.
18 Wireless sensor platforms can be used to collect and return data, but their performance in deep and
19 fast-moving ice requires quantification. We report experimental results from Cryoegg: a spherical
20 probe that can be deployed into a borehole or moulin and transit through the subglacial hydrological
21 system. The probe measures temperature, pressure and electrical conductivity in-situ and returns all
22 data wirelessly via a radio link. We demonstrate Cryoegg's utility in studying englacial channels and
23 moulins, including in-situ salt dilution gauging. Cryoegg uses very high frequency (VHF) radio to
24 transmit data to a surface receiving array. We demonstrate transmission through up to 1.3 km of cold
25 ice - a significant improvement on the previous design. The wireless transmission uses Wireless M-Bus
26 on 169 MHz; we present a simple radio link budget model for its performance in cold ice and
27 experimentally confirm its validity. Cryoegg has also been tested successfully in temperate ice. The
28 battery capacity should allow measurements to be made every two hours for more than a year. Future
29 iterations of the radio system will enable Cryoegg to transmit data through up to 2.5 km of ice.

30 INTRODUCTION

31 The presence and behaviour of liquid water in the subglacial environment governs the response of ice
32 to climate warming. Meltwater generated on the surface makes its way to the bed via networks of
33 moulins, cracks and crevasses (Chu, 2014; Flowers, 2018). Once at the bed, it flows to the ice margins
34 either through a subglacial drainage network consisting of inefficient linked cavities (Iken and
35 Bindschadler, 1986; Walder, 1986; Kamb, 1987), efficient channels carved into rock, ice or the
36 sediment below (Röthlisberger, 1972; Nye, 1976; Clarke, 1987; Ng, 2000), or a combination of both
37 (Hoffman and others, 2016). The configuration of the drainage network determines the subglacial
38 water pressure and how much of the ice-bed interface is in contact with liquid water. Contact
39 promotes sliding (Kamb, 1970; Iken, 1981; Schoof, 2010), which in turn can cause ice to accelerate
40 downstream. In recent years, the relationship between meltwater supply and ice acceleration has
41 been reevaluated in light of observations from the margins of the Greenland Ice Sheet that
42 demonstrate a seasonal evolution of subglacial drainage systems (Chandler and others, 2013;
43 Tedstone and others, 2015) commonly observed in Alpine systems (Nienow and others, 2005). Early
44 in the melt season, an increased flux of meltwater is routed to the bed and the low capacity,
45 inefficiently linked cavity system is forced to expand, forming efficient channels that can transport
46 substantial volumes of water. This reduces the area of the bed in contact with water, and potentially

47 regulates the flow of ice (Sole and others, 2011; Tedstone and others, 2015; Nienow and others, 2017;
48 Flowers, 2018). The defining feature of these different drainage configurations is the water pressure:
49 channelised systems operate at lower pressure than linked cavities, thus measurement of the
50 subglacial water pressure can be used to determine the likely structure of the drainage system, and
51 hence the acceleration response of the ice to increased surface melt inputs.

52 In addition to water pressure, other parameters may provide clues as to the structure of the drainage
53 system, but distinction between drainage system types is challenging. Temperature can be used to
54 assess whether the bed is at the pressure melting point, and the residence time of water in the system
55 can be used, in conjunction with pressure, to assess how efficiently the meltwater transits the system.
56 Long residence times are common in linked cavity systems, which results in prolonged contact
57 between meltwater and subglacial sediment (Tranter and others, 2002). This promotes chemical
58 weathering and changes the composition of the meltwater, so meltwater chemistry is a good indicator
59 of drainage system structure. Chemical composition is challenging to assess in situ, but a
60 measurement of the total dissolved solids can be easily obtained via a measurement of electrical
61 conductivity (Hubbard and others, 1995).

62 These three parameters (pressure (P), temperature (T) and electrical conductivity (EC)) are relatively
63 easy to measure via electronic sensors and can thus be combined to provide information on subglacial
64 drainage that could not be detected from the surface. Measuring these parameters subglacially is,
65 however, extremely challenging, particularly beneath thick, fast flowing ice. Yet it is these fast-flowing
66 sectors that govern the response of large ice masses to climate warming, since they transfer significant
67 volumes of ice to the ocean (Pritchard and others, 2009; van den Broeke and others, 2016). Drilling
68 boreholes through a glacier to access subglacial hydrological channels is logistically demanding and
69 disturbs the system that is under study. Once boreholes are drilled, implanting cabled sensors is
70 possible, but ice motion causes cables to flex and eventually break (Iken and others, 1993; Doyle and
71 others, 2018). In fast-flowing ice, data capture is thus limited to days or weeks. An alternative method
72 is therefore required that can capture these relatively simple electrical measurements and return
73 them to the surface without requiring a physical connection. A wireless radio frequency (RF) system
74 is ideal and there is a long history of the use of RF propagation through ice (see Plewes and Hubbard,
75 2001 for a review).

76 Here, we present trials of Cryoegg, a wireless sensor platform for use in deep ice. The use of a radio
77 link for subglacial telemetry has been proven by the work of the Glacsweb programme (Martinez and
78 others, 2004; Hart and others, 2019) and the WiSe project (Smeets and others, 2012). Previous work
79 (Bagshaw and others, 2014) showed that a 'Cryoegg' concept was feasible, namely a spherical sensor
80 platform containing all sensor, radio and datalogger components that could fit in a standard borehole
81 and travel through subglacial meltwater pathways: the electronics could be made sufficiently
82 compact, and that the radio link worked through up to 500m of ice. However, the radio link design
83 chosen proved unsuitable for performance in very deep ice, so design improvements were required.
84 In this paper we describe the redesign of Cryoegg to give enhanced radio link performance and show
85 the outcomes of field trials at sites in Greenland and the Swiss Alps.

86 In order to measure subglacial hydrological properties in deep polar ice, the enhanced Cryoegg had to
87 meet or exceed the following engineering constraints:

- 88 • An outer diameter of 120 mm or less, to fit into a standard ice core borehole
- 89 • A radio link capable of reaching the surface through 2,500 m of ice, the mean bed depth in
90 central Greenland (Morlighem and others, 2017)
- 91 • Survive and measure water pressure of up to 250 bar (equivalent to a water column of 2,500
92 m)
- 93 • Measure temperature, typically in the range from -30 to 0 °C
- 94 • Measure EC, typically in the range from 2 $\mu\text{S cm}^{-1}$ to 250 $\mu\text{S cm}^{-1}$
- 95 • A battery life capable of sustaining one measurement every 12 hours for a period of one year

96 RADIO LINK DESIGN

97 The success of the instrument depends principally on the performance of the radio link. The 2012
98 design (Bagshaw and others, 2014) used a simple frequency shift keying (FSK) transmitter operating
99 on 151 MHz and demonstrated a maximum range of 500 m in wet ice. To achieve a greater range, we
100 investigated alternative frequencies and transmission schemes. The power of a radio wave
101 propagating in “free space” (e.g. in air or vacuum) reduces according to an inverse square law with
102 distance - known as “geometric attenuation”. When the propagating wave reaches a receiving
103 antenna, the ability of that antenna to extract power from the incoming wave is the “effective
104 aperture”, and this depends upon the wavelength of the incoming wave. Antenna performance is
105 more usually characterised using the antenna gain, which is the ratio of the antenna’s effective
106 aperture in the direction of the main beam to the effective aperture of an “ideal” isotropic antenna
107 that receives signals equally well in all directions..

108 These effects are collectively described by the free space path loss equation, sometimes known as the
109 Friis transmission equation, which describes how a radio link performs in free space. The equation
110 assumes that the antennas are optimally pointed at one another and that their polarisations match,
111 otherwise there are further losses associated with pointing error and polarisation mismatch. The
112 original paper (Friis, 1946) presents the equation in terms of effective aperture, and in linear units.
113 The more commonly used version quoted here is expressed in terms of antenna gain and uses decibel
114 units.

115 Equation 1, adapted from Griffiths (1987, p. 12), is the free space path loss equation in decibel units:

$$116 P_{rx} = P_{tx} + G_{tx} + G_{rx} - 20 \log_{10} \left(\frac{4\pi d}{\lambda} \right) \quad (1)$$

- 117 • P_{rx} is power at the receiver, in dBW (dB relative to 1 watt)
- 118 • P_{tx} is power transmitted by the transmitter, in dBW
- 119 • G_{tx} is the gain of the transmitting antenna, in dBi (dB relative to the performance of an
120 isotropic antenna)
- 121 • G_{rx} is the gain of the receiving antenna, in dBi
- 122 • d is the distance between the transmitting and receiving antennas in metres
- 123 • λ is the wavelength of the transmission.

124 The last term of Equation 1 is known as the “free space path loss” (FSPL) and combines the geometric
125 attenuation due to distance with the apparent wavelength-related attenuation caused by the effective
126 aperture of the antennas. Consequently, the free space path loss equation gives us the rule of thumb

127 that lower frequencies (longer wavelengths) appear to propagate further than higher frequencies.
 128 FSPL over 2500 m ranges from 70 dB at 30 MHz to 99 dB at 868 MHz (Table 1), depending on frequency.
 129

System	WiSe (Smeets)	eTracer, Cryoegg (2012), Glacsweb (2012 – present)	Glacsweb (2004 –2006)	LoRaWAN	Cryoegg (2019)
Frequency (MHz)	30	150	433	868	169
Distance (m)					
100	42.0	56.0	65.2	71.2	57.0
500	56.0	70.0	79.2	85.2	71.0
1000	62.0	76.0	85.2	91.2	77.0
1500	65.5	79.5	88.7	94.7	80.5
2000	68.0	82.0	91.2	97.2	83.0
2500	70.0	83.9	93.1	99.2	85.0

130 Table 1: Values of free space path loss in dB for several frequencies used by previous subglacial
 131 wireless transmission systems (Smeets and others, 2012; Bagshaw and others, 2014; Martinez and
 132 others, 2004; Hart and others, 2019), the industrial standard LoRaWAN (Low power Radio Wireless
 133 Area Network (About LoRaWAN® | LoRa Alliance®)) and the redesign of Cryoegg (see results section).
 134

135 FSPL applies to all radio links regardless of the propagating medium. However, where the medium is
 136 lossy the signal is further attenuated by the interaction between the wave and the medium. Ice is one
 137 such lossy medium. Whilst simple models can predict RF attenuation in pure ice, in reality, glacier ice
 138 is heterogeneous, varying in temperature, pore water and impurity content and it contains cracks,
 139 water pockets and debris. Ultra-high frequencies (UHF, 300 MHz–3 GHz) have been effective for
 140 transmission through deep, cold and uniform ice (Lewis and others, 2015), but any presence of water
 141 in this matrix quickly reduces success due to scattering and attenuative losses. The high frequency
 142 (HF, 3-30 MHz) and very high frequency (VHF, 30-300 MHz) bands have good penetration through ice,
 143 with wavelengths longer than typical englacial water bodies encountered along the transmission path
 144 (asserted by Smeets and others, 2012).

145 The attenuation of electromagnetic waves in glacial ice is reported in the study of high-energy
 146 neutrinos (Barwick and others, 2005; Barrella and others, 2011) as *attenuation length* (L_a) in metres.
 147 This is related to *attenuation coefficient* (α) in decibels per metre by Equation 2 (Barrella and others,
 148 2011):

$$149 \quad L_a = \frac{1}{\ln \sqrt{10 \frac{\alpha}{10}}}. \quad (2)$$

150 We can rearrange and simplify Equation 2 to convert attenuation length to attenuation coefficient in
 151 dB m⁻¹ (Equation 3). Some typical values of attenuation length are shown converted to dB per
 152 kilometre in Table 2.

$$153 \quad \alpha = \frac{20}{(\ln 10)L_a} \quad (3)$$

154

Attenuation length (L_α), metres	Attenuation coefficient (α), dB km ⁻¹
100	86.9
200	43.4
300	29.0
400	21.7
500	17.4
600	14.5
700	12.4
800	10.9
900	9.7
1000	8.7
1500	5.8
2000	4.3
5000	1.7

156 Table 2: Attenuation length and corresponding attenuation coefficient from 100 to 5000 m

157 Attenuation lengths determined experimentally vary slightly by frequency (Barwick and others, 2005),
 158 with lower frequencies generally having longer attenuation lengths (and hence lower attenuation
 159 coefficients). Mitigating against both free-space and ice-related losses therefore points towards the
 160 use of lower frequencies for radio links within ice. However, low frequencies imply long wavelengths,
 161 which in turn requires physically large antennas, as an efficient antenna needs to be at least $\frac{1}{4}$ of a
 162 wavelength long. The WiSe system at 30 MHz has a wavelength of 10 metres and used half-wavelength
 163 dipole receiving antennas which were five metres long (Smeets and others, 2012). Large antennas
 164 become impractical to work with in the field, and we had the additional challenge of needing to fit our
 165 transmitting antenna into the 120 mm diameter Cryoegg enclosure. Our previous work used 151 MHz
 166 (wavelength 2 m), which had given satisfactory performance and allowed the receiving antenna to be
 167 easily carried in the field. The very small size of the Cryoegg enclosure meant that there was limited
 168 value in going to higher frequencies as the benefits of having a better-matched transmitting antenna
 169 were far outweighed by the additional free-space and ice-related losses. We therefore looked for a
 170 system that could operate in the VHF band (30-300 MHz).

171 For frequencies in the VHF range (30-300 MHz) the attenuation lengths reported (Barwick and others,
 172 2005; Barrella and others, 2011) range from 200 m to 3000 m. We take the worst-case figure of 200
 173 m (43.4 dB km⁻¹) as our design criterion for working in warm, wet ice and 400 m (21.7dB km⁻¹) as a
 174 conservative estimate for cold, dry ice (Table 2).

175

176 **METHODS**

177 **Choice of transmission scheme**

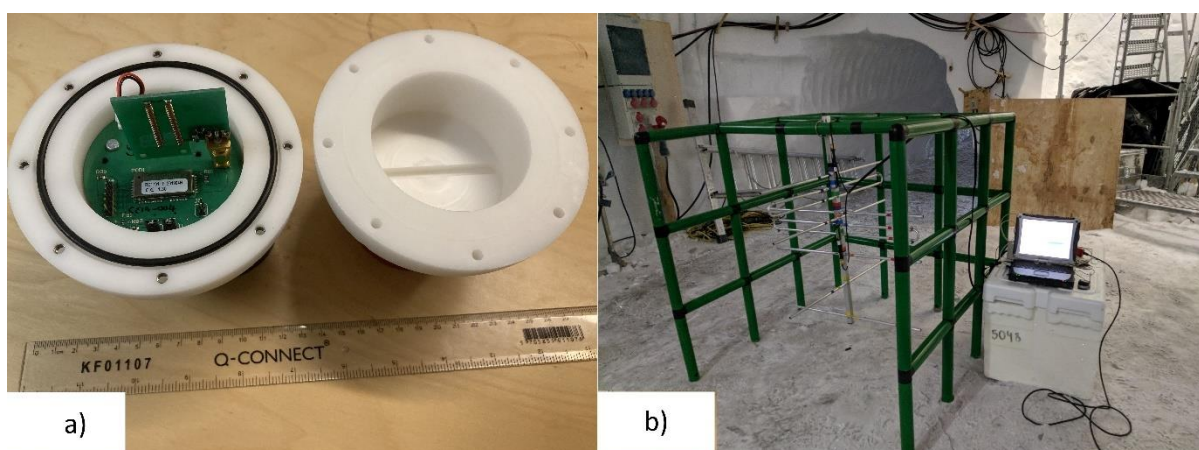
178 The term “transmission scheme” encompasses all the technical aspects of the radio link – the
179 modulation, error corrective coding, packetisation, and higher-level protocols. We required a
180 commercially available system designed for long battery life and for sending small amounts of data
181 over long distances, often sold as low power wide area networks (LPWAN) or “internet of things” (IoT)
182 systems. We selected Wireless M-Bus mode N1 (European Committee for Standardisation, 2013),
183 which is intended for use in utility metering. It is designed to offer very long battery life and sends
184 data at 2.4 kbit s⁻¹. It incorporates error corrective coding, which ensures that data received over the
185 link does not contain errors introduced in transit, and has optional cryptographic protection for
186 security. It operates on the 169 MHz frequency band, which is available for general license-free use in
187 Europe (CEPT ECC Recommendation 70-03). Wireless M-Bus is an open standard and a number of
188 manufacturers provide implementations of it. This gives confidence that the technology will remain
189 available, whereas a proprietary system carries a risk of the product being discontinued.

190 The Radiocrafts RC1701HP-MBUS4 modem used provides 0.5 W (27 dBm) power output on the 169
191 MHz band. One module is fitted to the printed circuit board (PCB) inside Cryoegg, configured as a
192 transmitter. For the receiver, we use Radiocrafts RC1701HP-MBUS4 demo kit with one board
193 configured as a receiver. This board connects to a PC and outputs the decoded data received over the
194 radio link. A Python script running on the PC applies a timestamp to the received packet data and
195 records it in a log file. This approach avoids the need to have a source of accurate time on board
196 Cryoegg.

197 **Antenna selection**

198 The transmitting antenna inside Cryoegg is constrained by the physical size of the spherical case. We
199 chose the HA.10 from Taoglas which is designed for the 169 MHz band, consisting of a pair of 30mm
200 long air-cored helical elements and a matching network. To minimise use of conductive materials
201 around the antenna, the upper hemisphere is devoted to the antenna and the remaining electronics
202 fit into the lower hemisphere (Figure 1a).

203



204

205 Figure 1 – a) Cryoegg with upper casework removed b) receiving antenna mounted on plastic frame

206 The receiving antenna on the surface provides additional gain to the system to help overcome the
207 attenuation through the ice, and to compensate for the small size of the transmitting antenna – an
208 ideal antenna would be 450 mm long, yet Cryoegg’s diameter is only 120 mm. We elected to use a

209 pair of crossed Yagi-Uda antennas (Innovantennas), which provide a gain of around 8 dB individually.
210 They are combined through a 90° hybrid combiner (Mini-Circuits part number ZMSCQ-2-180BR+)
211 which makes them behave as a single circularly polarised antenna, but at the expense of 3dB loss in
212 the combiner. By transmitting with linear polarisation and receiving with circular polarisation, we
213 make the radio link performance relatively independent of Cryoegg's orientation. This technique was
214 also used by the WiSe project team (Smeets and others, 2012).

215 The receiving antenna is one metre long. In order to minimise disturbance to the antenna pattern
216 caused by metal parts close to the antenna elements, we used a modular plastic frame (Quadro) to
217 support the antenna (Figure 1b).

218 The radiation pattern of Cryoegg was assessed in a screened RF test chamber (at the Wolfson Centre
219 for Magnetics in Cardiff) lined with absorbent ferrite material to prevent multipath. A log-periodic
220 antenna was used to receive the signal and the signal level was observed using a spectrum analyser in
221 peak hold mode.

222 Link budget

223 A link budget is used to evaluate whether an attenuation-limited radio link will work in practice.
224 Starting with the power output of the transmitter, gains and losses in the system are totalled up and
225 compared to the sensitivity of the receiver. To allow some margin for unexpected attenuation, we aim
226 for a received power level several dB higher than the sensitivity. Link budgets are traditionally
227 calculated in decibel units as this allows the gains and losses to be added and subtracted (rather than
228 multiplied and divided). Hence we use decibel units of power, such as dBW: decibels relative to one
229 watt, (0 dBW = 1W) or dBm: decibels relative to one milliwatt (0 dBm = 1mW = -30 dBW, and +30
230 dBm = 1 W = 0 dBW).

231 The link budget calculation (Table 3) assumes a 2000 m borehole through cold ice, with the
232 attenuation coefficient estimated at 21 dB km⁻¹. The performance of the transmit antenna was
233 relatively poor, and so we estimated its gain at -15 dBi (dB relative to an isotropic antenna) based on
234 data from the manufacturer. For the 2000 m example shown here, the received signal margin is 10.5
235 dB.

236

			Link budget contribution	Units
Transmitter power	0.5	W	27.0	dBm
Coupling loss			-0.5	dB
Transmit antenna gain			-15.0	dBi
Distance to receiver	2	km		
Frequency	169	MHz		
FSPL			-83.0	dB
Attenuation coefficient for cold ice	21	dB/km		
Ice related loss			-42.0	dB
Crosspolarisation loss			-3.0	dB
Receive antenna gain			8.0	dBi
Total power at receiver			-108.5	dBm
Receiver sensitivity	-119	dBm		
Margin			10.5	dB

238 Table 3: Link budget calculation for Cryoegg in 2000 m borehole in cold ice (gains are positive values,
239 losses are negative).

240 Sensors

241 The Keller PA-20D pressure sensor (max. 250 bar) has a vacuum-sealed membrane and communicates
242 with the microcontroller via the digital I²C interface (Inter-Integrated Circuit; (UM10204 I2C-bus
243 specification and user manual, 2014)). It provides internal temperature compensation, and supplies a
244 temperature reading alongside the pressure reading, although the manufacturer does not guarantee
245 its performance at temperatures below 0 °C. Hence we provided our own independent temperature
246 sensor (details below). The sensor provides a 16-bit pressure reading to the microcontroller but uses
247 only half the available range (the rest being used to allow it to report pressures slightly beyond the
248 calibrated range). This means that the smallest pressure step reportable is 7.6 millibars. The nominal
249 total error band is 1% of full scale, i.e. 2.5 bar, but in practice we found we could reliably record
250 changes in water pressure down to 0.1 bar (1m hydrostatic pressure) during field experiments.

251 The temperature and EC sensors are adapted from earlier designs (Bagshaw and others, 2012, 2014).
252 The EC sensor consists of a square wave oscillator which supplies a 500 kHz waveform to a potential
253 divider consisting of a precision resistor and a pair of sense electrodes. The sense electrodes are a pair
254 of M3 stainless steel hex-headed bolts that protrude through the case. The AC waveform from the
255 midpoint of the potential divider passes through a precision rectifier and RC filter to produce a DC
256 voltage that varies inversely with EC between the sense electrodes. This is sampled by the
257 microcontroller's analogue-to-digital converter (ADC) and the resulting digital value is reported over
258 the radio link. The temperature sensor is a Pt1000 platinum resistance device, used in a full-bridge
259 configuration with three fixed resistors. It is driven by a current source and measured using an
260 instrumentation amplifier, with the output fed to the microcontroller's ADC. Cryoegg reports the
261 digital value from the ADC over the radio link, allowing calibration to be carried out externally. The
262 Pt1000 resistor is mounted to the back of one of the EC sense electrodes with a thermal pad, ensuring
263 that it has thermal but not electrical contact.

264 **Microcontroller selection**

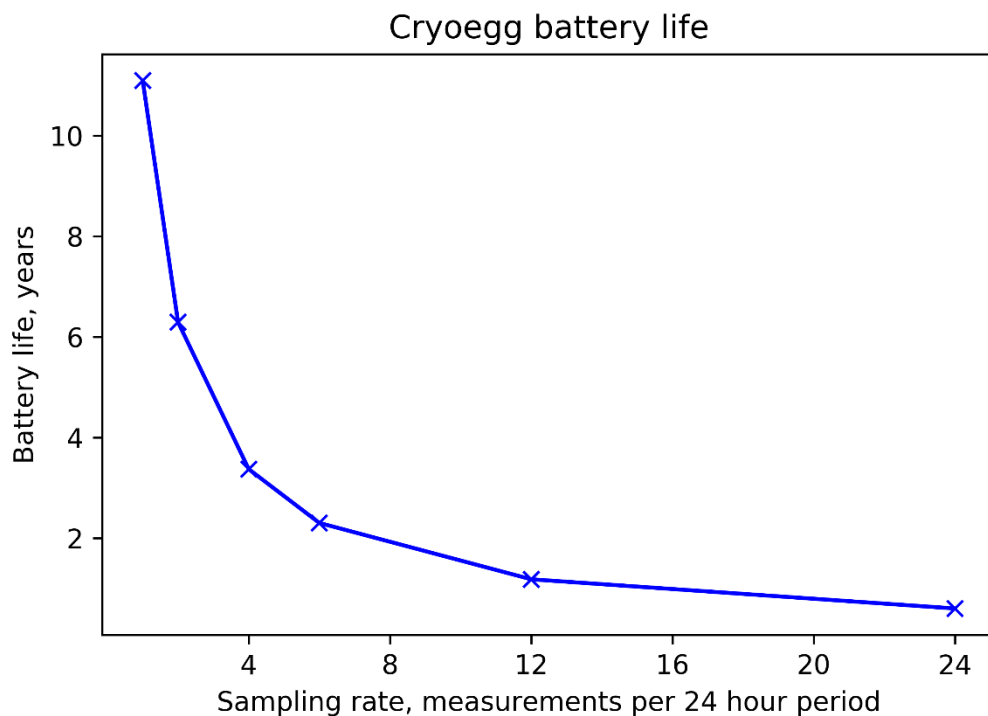
265 To maximise battery life, Cryoegg has a “sleep” mode where most subsystems were powered down
266 between measurements. The STM32L433RCT6P microcontroller (STMicroelectronics) has a built-in
267 Real Time Clock module (RTC) which uses an external quartz crystal oscillator to provide reliable
268 timekeeping at very low power. This “wakes” the microcontroller when it is time for the next
269 measurement. The RTC draws around 500 nA at 3.3 V with the rest of the microcontroller shut down.
270 The microcontroller has a 32-bit ARM Cortex M4 processor that can be clocked at up to 80 MHz, 256
271 kB of flash memory and 64 kB of RAM, and includes the ADC for the temperature and EC sensors; I²C
272 interface for the pressure sensor; and Universal Asynchronous Receiver/Transmitter (UART) for
273 communicating with the radio module. It also controls several power switches that enable and disable
274 power to other parts of the circuit.

275 **Power supply design and power consumption**

276 The radio modem module has relatively high power consumption during transmit – requiring 500 mA
277 at 3.3 V for less than 500 ms during each transmission, which puts a lot of demand on the battery and
278 power supply to be able to supply this peak current. A lithium-polymer rechargeable pouch cell can
279 supply sufficient peak current and be recharged between tests. The battery selected has a 3.7 V
280 nominal voltage and a capacity of 400 mAh.

281 A regulator IC with an enable input (ON Semiconductor NCP115ASN330T2G) supplies 3.3 V to the
282 sensors when enabled, and also provides the ADC reference voltage to the microcontroller. Other
283 parts of the circuit are supplied with unregulated battery voltage.

284 To estimate the battery life, we measured the power consumption of Cryoegg during transmission and
285 during sleep mode in the lab, using a logging multimeter (Mooshim Engineering Mooshimeter) that
286 could measure voltage and current from the battery simultaneously. The measure-and-transmit cycle
287 takes 3.2 seconds and consumes 0.5 J. The sleep mode current consumption proved to be too low for
288 the meter to measure (the lowest current it can record is 5 μ A). We therefore assume that the sleep
289 mode current consumption is that of the microcontroller only (since everything else is disabled) and
290 take the value quoted in the microcontroller datasheet of 500 nA.



291

292 Figure 2 - Cryoegg projected battery life with varying sampling rate

293

294 The projected battery life based on these measurements is over 6 years at two measurements per
 295 day. Even allowing for some self-discharge in the battery, this gives scope to increase the
 296 measurement frequency. A measurement every 2 hours (i.e. 12 times per day) gives a battery life of
 297 just over a year. Battery life estimates at different sampling rates are shown in Figure 2. Table S1 in
 298 the Supplementary Information shows an example battery life calculation in more detail.

299 **Mechanical design**

300 We aimed to provide a simple and robust mechanical design that was straightforward to assemble for
 301 testing. The spherical casework is machined in two halves from acetal copolymer, a hard engineering
 302 plastic (Figure 1a). The sensor PCB sits directly onto the bottom of the cylindrical internal void and is
 303 secured in place by two M3 threaded spacers, then potted with Raytech Liquid Rubber. There are two
 304 further PCBs that mount above the sensor PCB, which interconnect using multiway connectors. The
 305 processor PCB contains the microcontroller and associated components, and also provides mechanical
 306 support for the battery. The radio PCB is uppermost and supports the radio module, antenna
 307 connector, battery connector and headers for programming and debugging. The pouch cell battery is
 308 sandwiched in the gap between the radio and processor PCBs. The antenna PCB connects to the radio
 309 PCB via an SMA connector and is supported by a groove in the crown of the upper hemisphere. This
 310 design allows the upper hemisphere to be easily removed for access to the electronics, and to connect
 311 the battery before deployment. The upper and lower hemisphere seal with a rubber O-ring and are
 312 held in place by eight machine screws.

313

314 **Software**

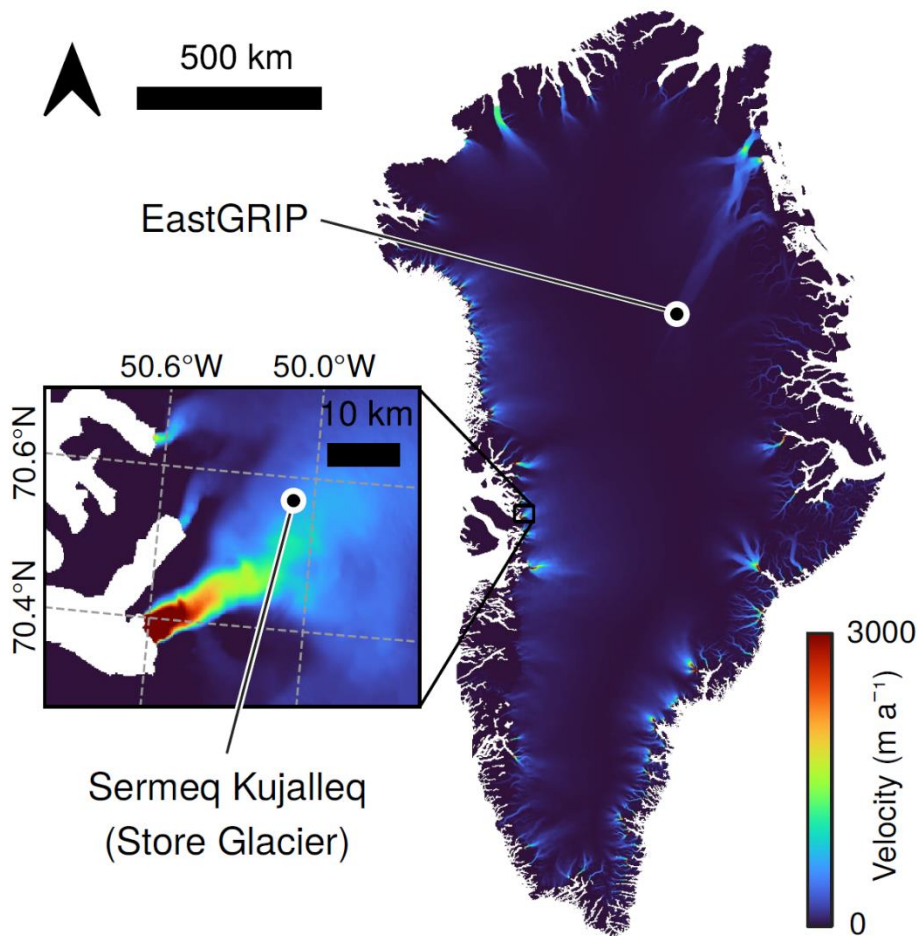
315 The software on the Cryoegg microcontroller is written in C, using the STM32 Hardware Abstraction
316 Libraries. The software goes through the following steps:

- 317 • Power up the sensors
- 318 • Make measurements
- 319 • Power down the sensors
- 320 • Power up the radio module
- 321 • Pack the sensor data into a data packet
- 322 • Send the data packet to the radio module to be transmitted
- 323 • Power down the radio module
- 324 • Set the sleep timer for the next measurement
- 325 • Enter deep sleep (“SHUTDOWN”) mode

326 On awakening from SHUTDOWN mode, the program restarts from the beginning, thus giving an
327 endless loop. The measurements are transmitted immediately after being made, and no data is stored
328 on Cryoegg, since we do not expect to retrieve Cryoegg after deployment.

329 **Field testing**

330 We conducted three field tests during July and August 2019 at two sites in Greenland (EastGRIP drill
331 site and Sermeq Kujalleq/Store Glacier) and one in Switzerland (Rhône Glacier). The objectives of the
332 field tests were to verify the operation of Cryoegg and its receiver in a real glacial environment. We
333 wanted to demonstrate the operation of the radio link in both cold deep ice and shallower temperate
334 ice, and confirm the mechanical integrity of the device when subjected to hydrostatic pressure in fluid-
335 filled boreholes.



336 Figure 3 - Velocity map of Greenland ice sheet flow, showing locations of EastGRIP and Sermeq
 337 Kujalleq test sites in fast flowing ice. Data from MEaSURES dataset of annual Greenland velocity for
 338 2018 (Joughin and others, 2010; Joughin, 2017).

339 *East Greenland Ice Core Project site (EastGRIP)*

340 EastGRIP is located at N75° 38.05' W036° 00.22' on the North East Greenland Ice Stream (NEGIS), the
 341 largest ice stream in Greenland, which drains 340,000 km² of the ice sheet and extends for over 1000
 342 km inland (Figure 3). Approximately 150 km from the onset, it reaches speeds of 65 m a⁻¹ (Joughin and
 343 others, 2010; Karlsson and Dahl-Jensen, 2015). The East Greenland Ice core Project (EastGRIP) is a
 344 unique project drilling an ice core into 2.5 km of fast flowing ice to investigate ice stream beds
 345 (www.eastgrip.org). In summer 2019, the core had been drilled to 2 km depth, leaving behind a 2 km
 346 borehole filled almost completely with drill fluid. The purpose of our field trial at this site was to obtain
 347 a range test for the radio link and a pressure test for the mechanical design. Cryoegg was deployed in
 348 a mesh bag and attached to the main winch (Figure 4). The orientation of Cryoegg within the bag was
 349 not fully controlled due to its spherical shape, although the pressure sensor protruding through the
 350 mesh helped to prevent it from shifting. The receiving antenna was set up in the drill trench, close to
 351 the winch (Figure 1b). Cryoegg was lowered and raised into the borehole several times and the
 352 received signal strength (RSSI) and live data stream monitored at the surface, adjacent to the top of
 353 the borehole.



354

355 Figure 4 – Cryoegg ready for deployment on the EastGRIP ice core winch.

356

357 *RESPONDER site at Sermeq Kujalleq*

358 We tested Cryoegg at an inland site (N70° 33.889' W50° 04.558') at Sermeq Kujalleq (Store Glacier),
359 the third fastest outlet glacier in West Greenland (Figure 3). It has a catchment of 35,000 km² that
360 includes supraglacial lakes that periodically drain via cracks and moulins, several on an annual basis
361 (Chudley and others, 2019). The glacier experiences changes in ice flow associated with sudden
362 injections of meltwater to the pressurised drainage system (Doyle and others, 2018), but the link
363 between surface lake drainage and the subglacial hydrology is poorly defined, primarily because
364 instrumenting a draining lake with cabled sensors is near-impossible. There is extensive supporting
365 data available on the subglacial bed structure, lake drainage frequency and ice strain rates (Hofstede
366 and others, 2018; Young and others, 2018; Chudley and others, 2019). Sermeq Kujalleq is the site of
367 the RESPONDER project, offering access to the glacier bed through hot water drilling. The glacier is
368 approximately 1 km thick at this site (Morlighem and others, 2017), and bed access holes were hot
369 water drilled in July 2019.

370 A surface propagation test assessed the range of data transmission through air by monitoring the RSSI
371 and live data stream as the receiving antenna was deployed at a fixed site and Cryoegg hand-carried
372 over a distance of 1.6 km. A hand-held GPS receiver was used to record the position of Cryoegg as it
373 was carried, and the fixed position of the Cryoegg receiver.



375

376 Figure 5 – topographic map of Switzerland showing location of the Rhône Glacier

377

378 The Rhône Glacier is located at N46°34.32' E8°22.58' in the Swiss Alps and is one of the most studied
379 glaciers, with records of front position dating back to the 17th Century (Church and others, 2019). The
380 16 km² glacier is at the pressure melting point throughout and there is an active subglacial drainage
381 network. The glacier is the focus of an intensive subglacial monitoring project, with artificial moulins
382 drilled via hot water in 2018. The moulins remained active in August 2019, when we deployed Cryoegg
383 on the end of a rope tether.

384 Salt dilution gauging (Moore, 2005) was used to estimate moulin discharge. A known quantity of
385 tracer, sodium chloride (NaCl, “table salt”) was added to the supraglacial stream approximately 25 m
386 upstream of the moulin. The discharge can then be calculated from EC readings and the concentration
387 of NaCl added. EC was measured in the supraglacial stream by a Keller DCX-22-CTD 15 m upstream of
388 the moulin and also recorded and transmitted once per second by a Cryoegg lowered into water at
389 the bottom of the moulin.

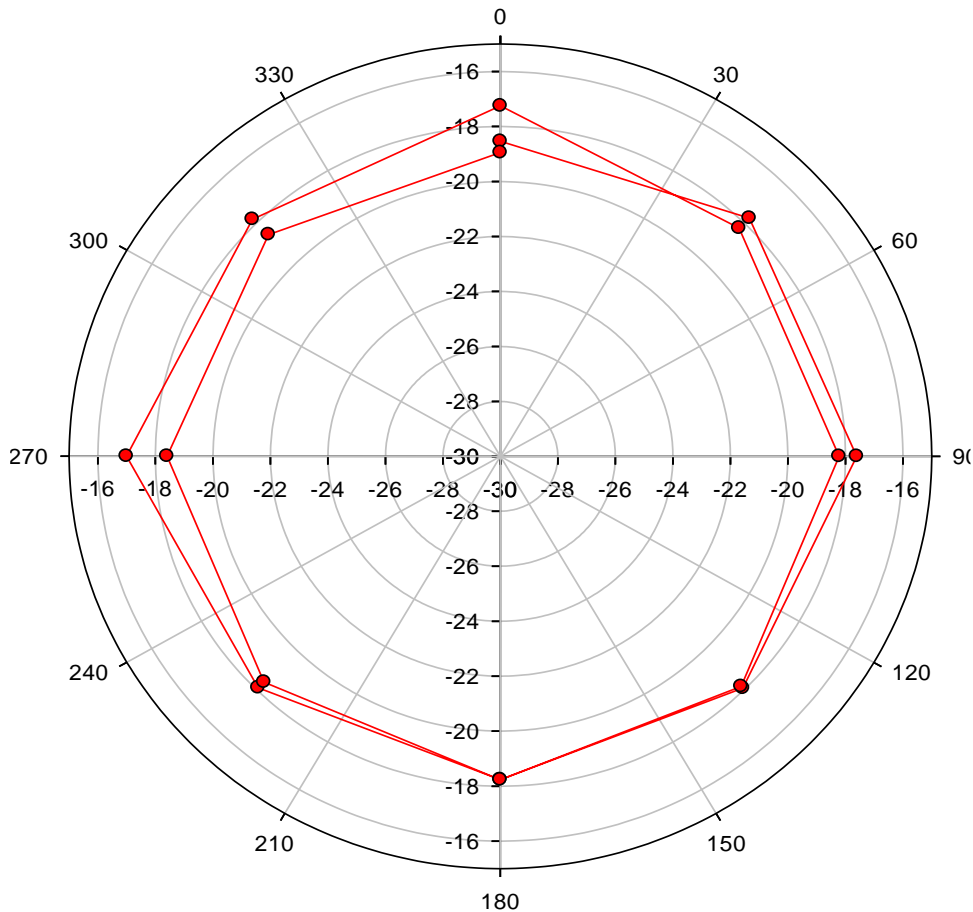
390

391 **RESULTS**

392 **Laboratory RF tests**

393

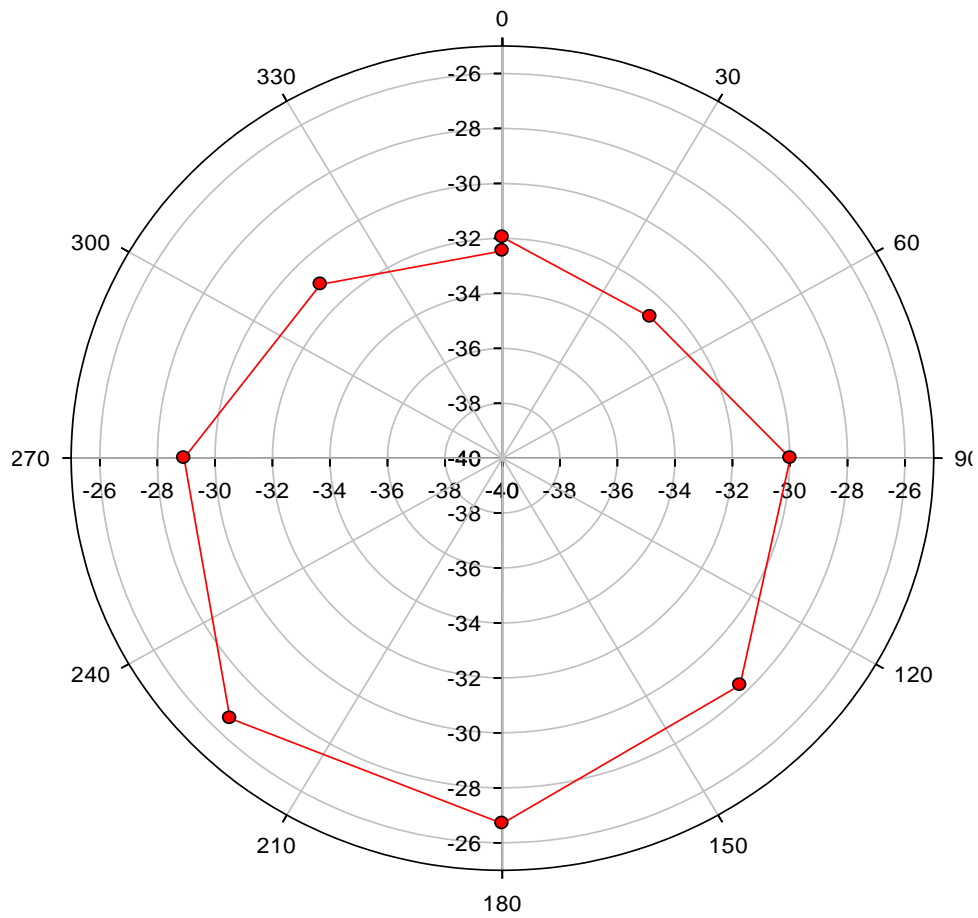
394 RF power meter assessments confirmed that the transmitter put out the full +27 dBm (0.5 W) during
395 each transmission.



396

397 Figure 6 – Horizontal radiation pattern of Cryoegg measured in the RF test chamber

398 The horizontal radiation pattern was measured at eight points around the circumference and is shown
399 in Figure 6. For this measurement the receiving antenna (a log-periodic) was vertically polarised (a
400 brief check showed that this gave a larger signal than when horizontally polarised) and Cryoegg was
401 orientated with its case split line horizontal. Two complete revolutions were measured to check
402 consistency, and it is clear that the pattern is largely omnidirectional, varying by < 2 dB.



403

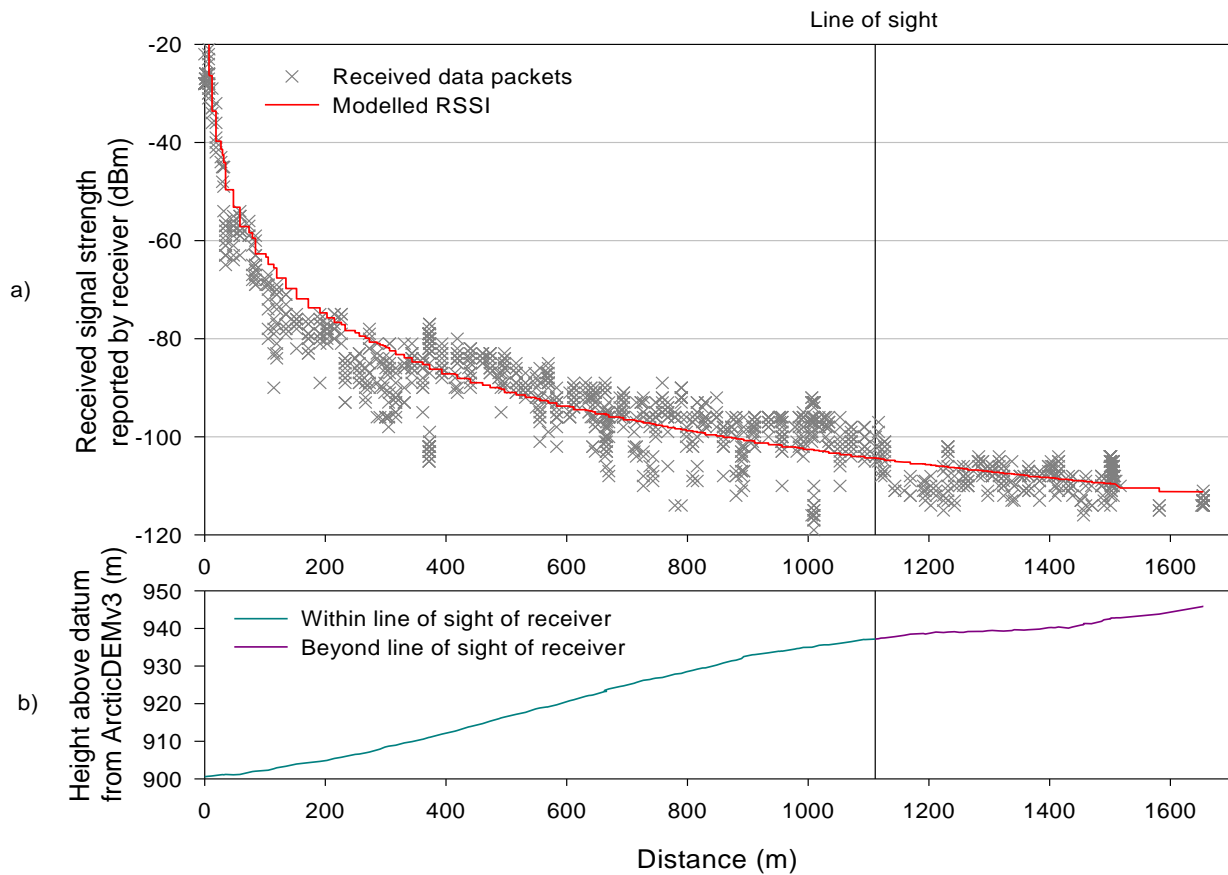
404 Figure 7 – Vertical radiation pattern of Cryoegg measured in the RF test chamber

405 To simulate the RF performance in the borehole, we re-oriented the Cryoegg to have the same
 406 orientation as it would have in the borehole, with the split line vertical and normal to the receiving
 407 antenna boresight – i.e. with the crown of the upper half pointing towards the receiving antenna, and
 408 the sensor ports pointing away. The receiving antenna was vertically polarised. The results in Figure 7
 409 show that the signal level is significantly lower (10-12 dB) than in the horizontal plane, and that the
 410 pattern is not omnidirectional; there is a 6 dB variation as the unit is rotated.

411

412

413 Surface propagation at Sermeq Kujalleq



414

415 Figure 8 – a) RSSI recorded by receiver during surface range test at Sermeq Kujalleq and modelled
 416 received signal strength.). b) shows the ground elevation along the route taken. The black vertical line
 417 in both plots shows the point where the transmitter went beyond the line of sight to the receiver due
 418 to the glacier surface topography.

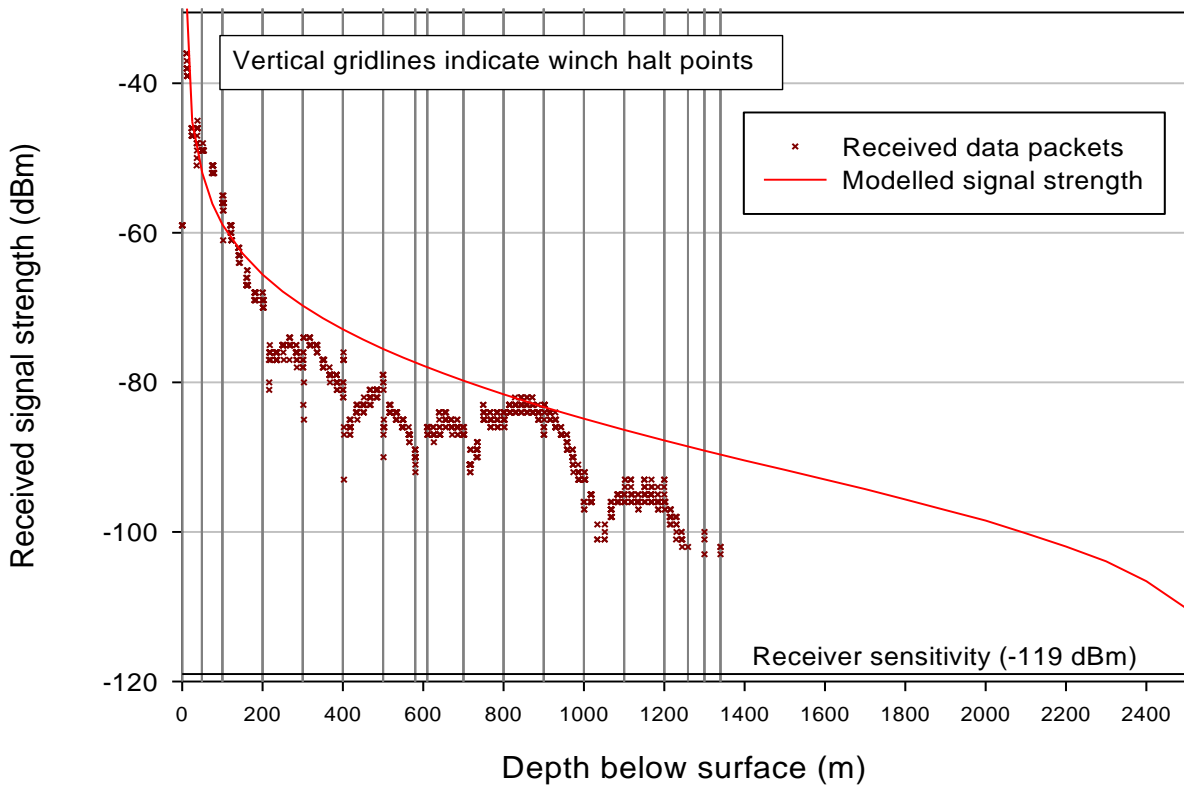
419 Figure 8a shows recorded signal strength for successfully received data packets against range from
 420 the receiver. The terrain profile in Figure 8b was produced from ArcticDEM v3 (Porter and others,
 421 2018) 2 m mosaic values extracted to match the GPS positions recorded in the field. A line of sight
 422 binary was calculated using the QGIS visibility analysis plugin with the receiver height set at 1.5 m and
 423 the transmitter height at 1 m.

424 **Deployment at Sermeq Kujalleq**

425 Cryoegg was lowered into a hot water drilled borehole and a moulin. One deployment attempt was
 426 made in the hot water drilled borehole, but the borehole proved too narrow for Cryoegg to pass
 427 through. One data point was obtained with Cryoegg in the borehole about 400 m below the surface,
 428 but it was impossible to proceed further because of borehole refreezing. Moulin deployment was
 429 attempted in a very large moulin (measured at $4.3 \text{ m}^3\text{s}^{-1}$ discharge at the time of deployment) adjacent
 430 to the drill site. Cryoegg was caught in a series of plunge pools and eventually the force of the water
 431 caused it to break free from its tether and it was rapidly swept away out of range. We only obtained
 432 a few data points before losing the signal.

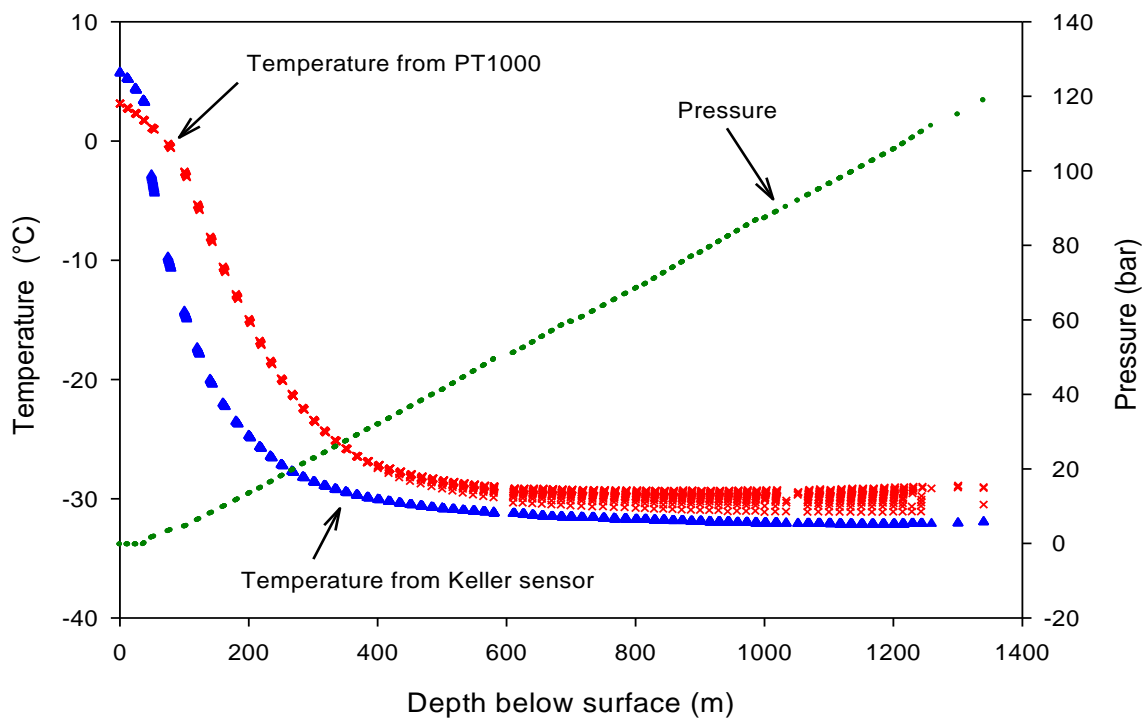
433 **Downhole propagation at EastGRIP**

434 At EastGRIP, the borehole is filled with ESTISOL 240 drill fluid rather than water (Sheldon and others,
435 2014). Previous tests at the site (Bagshaw and others, 2018) demonstrated that the fluid had minimal
436 impact on signal propagation. Figure 9 shows the RSSI plotted against depth. Depth is linearly
437 interpolated between depth-measured winch halt points (shown as vertical gridlines on Figure 9),
438 which is a fair assumption because the winch motor speed was constant between these halts. The
439 firmware was configured to produce a burst of 16 packets, one per second, and then wait for 60
440 seconds before the next burst. This accounts for the clustered data points on Figure 9, as all the
441 successfully received packets are plotted. There are large variations (>10 dB) in signal level at 300, 400
442 and 500 m, coinciding with the point where the winch was halted, and even retrograde paths, for
443 example between 400 and 500 m; 700-850 m; 1000-1100 m. The deepest point at which packets were
444 successfully received was 1340m below the surface. No packets were received as Cryoegg was pulled
445 back up to the surface. When Cryoegg was retrieved, it was found to be full of drill fluid, indicating
446 that it had leaked under pressure.



447

448 Figure 9 – Received signal strength of successfully-received data packets during a test in the
449 EastGRIP borehole, together with modelled signal strength (explained in “radioglaciological
450 implications” section)



451

452

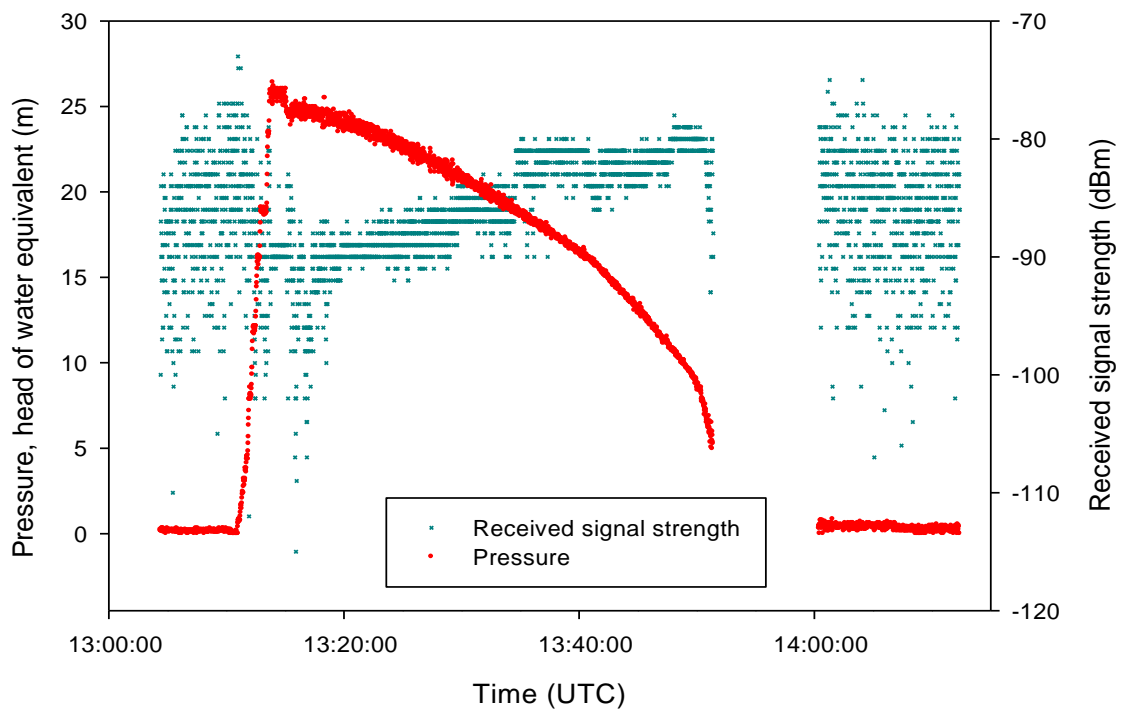
453 Figure 10 – Cryoegg sensor data received at the surface during deployment into the EastGRIP
 454 borehole.

455 The hydrostatic pressure increased with depth (Figure 10) – the small offset is because the drill fluid
 456 is around 50 m below the surface level. Data was obtained down to 1340 m, although significant
 457 packet loss occurred beyond 1250 m. The two temperature plots represent data from the two
 458 different temperature sensors. The Pt1000 sensor is inside the case, hence it records a higher
 459 temperature for a given depth when compared with the Keller, which has direct contact with the drill
 460 fluid. The conversion equation from the Pt1000 reported value (which is in arbitrary units) to
 461 temperature is based on theory and has not been confirmed by calibration. The high degree of
 462 clustering of the data points from the Keller sensor suggests that it contains some internal averaging,
 463 although this may be caused by the significant mass of the sensor body itself. Cryoegg was at ambient
 464 ice surface temperature before entering the borehole, so the majority of the temperature data
 465 recorded here is simply the instrument cooling down to the ambient englacial temperature. The
 466 spread in Pt1000 temperature results beyond 400m depth is caused by self-heating of the sensor due
 467 to repeated measurements in quick succession, which becomes apparent once Cryoegg has cooled to
 468 the ambient englacial temperature.

469

470 Moulin drainage at Rhône Glacier

471 Cryoegg was not able to reach the bed of the Rhône Glacier, 200m below the surface, via the moulin
472 and instead appeared to be in a deep plunge pool 150m below the surface. Pressure readings received
473 from Cryoegg in real time confirmed that it was in up to 25m deep water. Figure 11 shows the pressure
474 recorded whilst Cryoegg was in the plunge pool, and the corresponding received signal strength. There
475 was a sharp rise in pressure as Cryoegg was lowered into the water at 13:12:00 UTC and then a gradual
476 decline over the next 40 minutes. The gap in the data centred on 13:55 was an interruption in the data
477 logging. After the logging resumed, the water pressure had fallen to atmospheric pressure. The
478 reduction in water pressure coincided with a 10dB increase in received signal strength over the same
479 period.



480

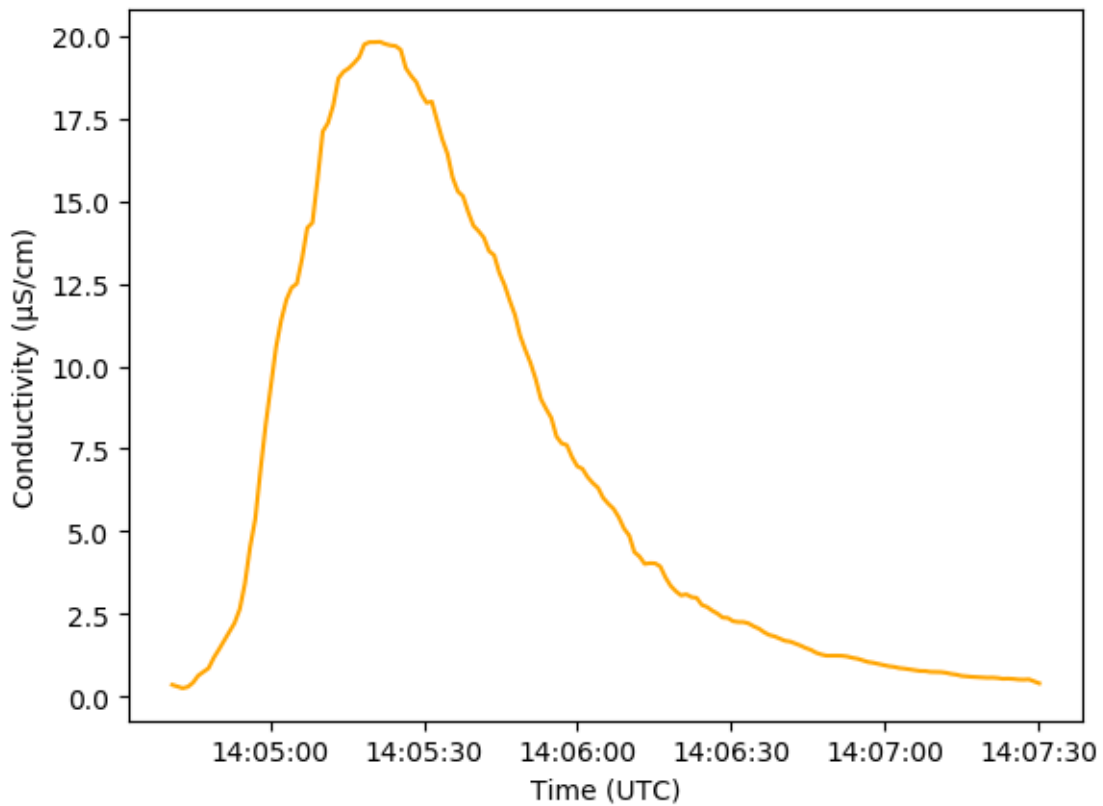
481 Figure 11 – Pressure and received signal strength from Cryoegg in a moulin on Rhône Glacier, 15th
482 August 2019

483

484

485 Salt discharge gauging at Rhône Glacier

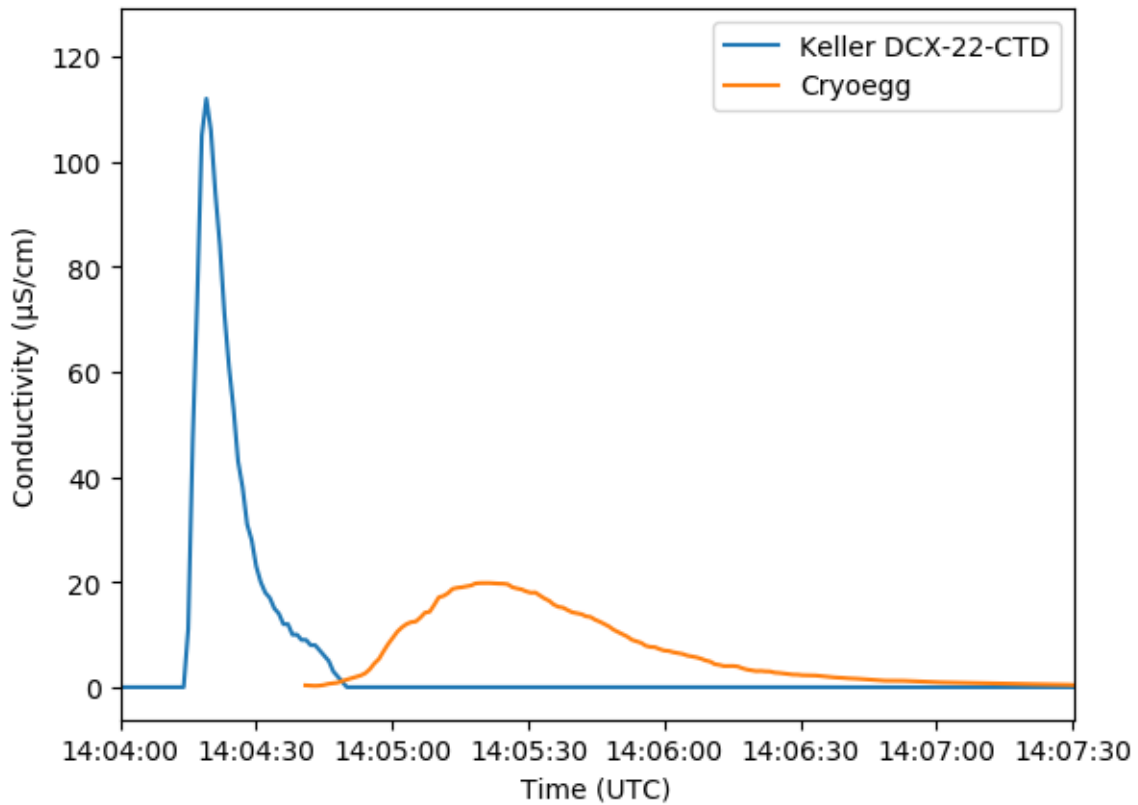
486 Figure 12 shows an example of EC changes as a salt wave passes the Cryoegg, transmitted in real time
487 from the moulin plunge pool at 150 m below the ice surface.



488

489 Figure 12 – reported EC from Cryoegg from within a moulin on Rhône Glacier during a salt slug
490 injection test, 15th August 2019.

491 Simultaneously, the Keller DCX-22-CTD in the supraglacial streams that fed into this same moulin
492 measured the injection of the 100 g l⁻¹ NaCl salt solution 10 m upstream from the logger. Figure 13
493 shows the results from the Keller logger in the stream alongside the results from Cryoegg in the
494 moulin.



495

496 Figure 13 – comparison of salt wave passing Keller logger in the supraglacial stream with Cryoegg
 497 within the moulin. 15th August 2019.

498 The discharge of the supraglacial stream was calculated by the salt dilution as 104 litres s⁻¹ (Moore,
 499 2005), and the discharge within the moulin was slightly higher at 113 litres s⁻¹. The time between the
 500 two peaks was 60 seconds. The velocity of the water between the two instruments was 2.75 m s⁻¹
 501 based on the transit time and the distance between them (15 m in the stream + 150 m down the
 502 moulin = 165 m).

503

504 DISCUSSION

505 Radioglaciological implications

506 The main objective of field testing was to verify the performance of Cryoegg in a real glacial
507 environment. The surface range test at Sermeq Kujalleq (Figure 8) confirmed that the radiated output
508 of Cryoegg matched our design calculations. We modelled the expected RSSI using the conventional
509 two-ray ground-reflection model (Bullington, 1947) used for VHF propagation. The transmitter and
510 receiver heights required were modelled using the DEM profile shown in Figure 8b. The transmitter
511 and receiver parameters in the model were those from the link budget in Table 3. The model produces
512 a good fit to the real data, confirming that the parameters were indeed realistic estimates. The
513 variations in the data are because the DEM profile is an average of the glacier surface terrain, and in
514 practice the glacier surface was not flat. The later part of the test was beyond the line of sight to the
515 receiver (as shown by the elevation profile in Figure 8b), which accounts for the step reduction in
516 signal strength beyond 1100 m.

517 The test in the EastGRIP borehole was intended to verify both the mechanical and electrical
518 performance of Cryoegg in a simulated deployment, and demonstrate the radio link through deep
519 glacial ice. No data was received beyond 1340 m depth and on return to the surface Cryoegg was
520 found to have failed and stopped transmitting. This appears to have been a mechanical failure. Drill
521 fluid was found in the Cryoegg housing after the tests. The fluid is non-conductive and so should not
522 have caused any electrical damage, but the hydrostatic pressure is likely to have affected the some
523 components. The most likely failure points are the battery (which being a soft “pouch cell” type has
524 no protection from pressure) and its connectors, which may be forced apart by non-conductive fluid
525 under high pressure, breaking the circuit.

526 An important question remains: if the leak had not occurred and Cryoegg had continued operating
527 down to the bottom of the borehole (2000 m down), would we have received data at that depth? To
528 determine this, we estimate the RF performance based on the recorded data.

529 The receiver sensitivity (the minimum decodable signal strength) is -119 dBm (1.25 fW), and in other
530 range tests (Figure 8) we succeeded in decoding signals down to this level (RC1701xx-MBUS
531 Datasheet, 2018). However, the RSSI data for the EastGRIP borehole (Figure 9) show that the weakest
532 signals received were at -103 dBm, 16 dB above the minimum receivable level. This suggests the
533 system would have continued working beyond 1340 metres depth without the mechanical failure. To
534 forecast signal levels at greater depth, we modelled the RF performance in the borehole. The initial
535 link budget (Table 3) overestimates the RSSI in the borehole, even at points very close to the surface,
536 suggesting that the radiated signal from Cryoegg was much lower in the borehole when compared to
537 the surface range test. It is likely that the antenna performance was affected by the substantial metal
538 apparatus on the winch cable just above where Cryoegg was attached. The dielectric constant of the
539 drill fluid is not the same as in air and this may also have affected the antenna matching. Consequently,
540 reducing the transmit antenna gain by 20dB (to -35dBi) produces a model result that more closely fits
541 the data.

542 The temperature profile of the EastGRIP borehole was measured in July 2019 using the University of
543 Copenhagen’s automated logger (Gundrestup and others, 1994), and so our radio propagation model
544 was revised to incorporate the temperature-dependent attenuation of the ice. We applied the
545 temperature measurements to an attenuation model (MacGregor and others, 2007, 2015) to give an
546 estimate for the ice-related attenuation down to 2100m below the surface (Figure 9). To continue the
547 temperature profile to the glacier bed depth (2500m) we conjectured that the temperature would rise
548 rapidly to reach 0 °C at the bed, by analogy with the temperature profile at NorthGRIP (Dahl-Jensen

549 and others, 2003). This represents a worst-case since the model produces very high attenuation (69
550 dB km⁻¹) at 0 °C. This produces a profile with relatively low attenuation (~7dB km⁻¹) in the coldest part
551 of the glacier, increasing rapidly at the surface and bed where the ice is warmer.

552 The modelled signal strength is higher than the real data at most depths (Figure 9), although it matches
553 the peak between 800 and 900 m, and there are two further effects that help explain why.

554 Firstly, the large (>10 dB) variation in signal strength observed at several winch halt points is most
555 likely caused by Cryoegg rotating on the vertical axis as the wire rope twists. Cryoegg was oriented
556 with its split line horizontal during these tests, meaning that the transmitting antenna is oriented in
557 an end-fire mode towards the receiver. The deceleration of the winch will result in some of the
558 momentum of Cryoegg and the cable being converted into torsional forces on the winch cable, with
559 Cryoegg twisting back and forth on the end of the cable. This will affect the radiation from the antenna
560 because the radiation pattern seen by the receiving antenna is not uniform (Figure 7). It is plausible
561 that the retrograde slope of the signal strength between 400 and 500m is caused by Cryoegg slowly
562 rotating on the winch cable, given the signal variation is comparable to that seen during the 400m and
563 500m winch halts.

564 Secondly, the signal strength plot (Figure 9) also appears to show a number of nulls – locations where
565 the signal strength drops significantly – notably at around 600 m and 1040 m. Nulls are often produced
566 by multipath reflection effects, such as when the signal reflected off a surface interferes destructively
567 with the direct signal at the receiver (Griffiths, 1987, 102–104). However, in this case there is no
568 obvious candidate for the reflecting surface: the geometry required to produce widely-spaced large
569 nulls rules out horizontal reflectors like the glacier bed or internal layers. The shear margin is too far
570 away (5 km) to produce this type of null. These effects can be explained by birefringence: glacier ice
571 has previously been shown to affect the polarisation of VHF radio waves (Hargreaves, 1978; Li and
572 others, 2018). Birefringence splits the wave from Cryoegg into two elliptically-polarised waves of
573 opposing chirality with differing phase velocities. The relative phase delay between the two waves
574 appears at the receiver as an apparent change in polarisation, and therefore it is possible that the
575 wave could arrive at the receiving antenna on the opposite polarisation to the antenna, resulting in a
576 null. Since this phase delay relates to distance travelled through the medium, this effect would
577 produce nulls at specific depths corresponding to relative phase delays of 180 degrees.

578 The axial rotation of Cryoegg and the birefringent effects may also act in concert, which would explain
579 why the signal variations are so large at some of the winch halt points (>10 dB at most locations).
580 These two effects explain why the signal level drops below the modelled values: the model assumes
581 constant antenna gain and matched polarisation, whereas in the real data the orientation varies
582 (altering the transmit antenna gain) and the birefringence means that a proportion of the signal power
583 is transferred to the opposite polarisation and is lost to the receiver.

584 The birefringent effect could be mitigated against in future development by feeding the output of
585 each of the two crossed receiving antennas into a two-channel diversity receiver, which would then
586 be able to decode the signal regardless of its polarisation. This polarisation diversity technique has
587 previously been demonstrated mitigating polarisation nulls in HF ionospheric radio links (Stott, 2005)
588 where magnetoionic effects produce polarisation changes which are analogous to those produced by
589 birefringence (Davies, 1990). We hope to confirm this in future work.

590 The performance of the radio link in the Rhône glacier moulin (Figure 11) was satisfactory. We
591 anticipated that the temperate ice and presence of flowing water would increase the overall
592 attenuation. Figure 11 shows that the signal propagating through 25 m of meltwater and a further 125

593 m of temperate ice to the glacier surface was attenuated to -90 dBm. This compares with the EastGRIP
594 borehole (Figure 9) where this signal strength was reached after more than 500 m. The reduction in
595 observed moulin water pressure, indicative of 25m head of water draining out of the moulin, produced
596 an increase in RSSI by around 10 dB. This confirms that the presence of liquid water increases the
597 signal attenuation.

598 The variation in signal is much greater when Cryoegg is in the “atmospheric pressure” region of the
599 moulin rather than when it is in >1 m of water (Figure 11). When Cryoegg is reporting pressure close
600 to atmospheric pressure, it is being splashed by the water, or water is flowing smoothly past it. In this
601 scenario the water flow will spin and agitate Cryoegg on the end of the rope, creating variation in
602 signal level because of the antenna pattern. The turbulent flow of the water will also create ever-
603 changing levels of attenuation. However, once Cryoegg is below the water surface, the viscosity of the
604 water will reduce its spinning and agitation, and the attenuation due to the water will be constant.

605

606 Glaciohydrological implications

607 The water pressure recorded by Cryoegg in the moulin steadily decreased during the 40 minutes that
608 it remained in the plunge pool (Figure 11). Eventually, the water level dropped below the Cryoegg and
609 it returned to atmospheric pressure with the characteristic fluctuations in RSSI caused by splashing
610 water. We interpret this as dynamic drainage of the plunge pool over the afternoon, as water backed
611 up in the drainage system forces its way to the glacier bed. Similar pressure variations have been
612 previously observed in moulins (Iken, 1972; Röthlisberger, 1980; Holmlund and Hooke, 1983) and
613 demonstrate that the subglacial drainage system is not in equilibrium but constantly fluctuating
614 (Röthlisberger and Lang, 1987). The characteristic step-pool system develops if the moulin persists for
615 more than one season (Gulley, 2009); the artificial moulin was drilled directly to the end in 2018, but
616 by 2019 was 'kinked' and a plunge pool formed approximately 50 m above the bed.

617 Simultaneous salt tracing in a supraglacial stream feeding the moulin and within the moulin itself
618 shows (Figure 13) that the moulin discharge was slightly higher than the stream discharge –
619 unsurprising, as the stream that we measured was not the sole supply of water feeding the moulin.
620 This experiment demonstrates Cryoegg's potential for measuring hydrological parameters in locations
621 that are difficult to access. Previously, moulin discharge has been estimated at the surface (either by
622 field measurements or remote sensing), which masks the effect of water being stored within the
623 vertical column of the moulin itself (Werder and others, 2010). We show that it is possible to monitor
624 supraglacial discharge, the height of the stored water column within the moulin, and the moulin
625 discharge simultaneously and in real time, providing a valuable new approach for future studies of
626 glacier hydrology.

627 Comparison with other wireless subglacial probes

628 The most successful wireless subglacial probe for deep ice has been the WiSe system (Smeets and
629 others, 2012). This was demonstrated returning a signal through 2500 m of ice in Greenland. This
630 system operated at 30 MHz in order to benefit from lower free-space path loss, but at the expense of
631 making the antennas very large. The WiSe system suffered from some skywave interference affecting
632 signal reception, which is a particular issue at 30 MHz and below, and required use of a large (5 m
633 long) HB9CV type antenna to mitigate against it. WiSe required a 1 W (+30 dBm) transmitter to
634 communicate at depths of more than 2000 m, but it is not clear how much of this power was actually
635 radiated – the ferrite-loaded antenna used was likely to be very lossy.

636 The GlacsWeb system originally operated at 433 MHz (Martinez and others, 2004) but later (Martinez
637 and others, 2013) used 151 MHz, giving a maximum reported range in ice of 70 m (Hart and others,
638 2019). Cryoegg is specifically designed for deep ice, and hence its radio performance greatly exceeds
639 that of GlacsWeb, enabling its use in at least 1000 m of ice. Our probe and receiving antenna are both
640 more compact than the WiSe system and we use commercially-available radio modules that adhere
641 to an international open standard, which means that the key components are likely to be readily
642 available well into the future.

643

644 CONCLUSION AND OUTLOOK

645 We have undertaken a full re-design of the wireless subglacial sensor platform Cryoegg, using a new
646 radio link technology and improved link budget design, and demonstrate that it can transmit sensor
647 data in real time through more than 1.3 km of cold ice. Deployments in moulins in temperate ice show
648 that Cryoegg is a valuable tool for recording englacial and subglacial hydrological properties in situ,
649 and hence giving further insight into processes in these environments. The EC sensor, originally

650 intended as a proxy for total dissolved solids in subglacial water, can facilitate salt dilution gauging for
651 real-time estimates of discharge. All sensors operated well, revealing englacial conditions and
652 demonstrating their applicability for future subglacial deployments. The sensors fitted to the existing
653 design were chosen because of their ease of implementation and their applicability to studies of
654 subglacial hydrology, but Cryoegg can be adapted to support other sensors.

655 Future developments will refine and enhance the design, particularly with respect to the antenna
656 performance and mechanical design, so that we have a robust instrument capable of returning data
657 for months or years through 2.5 km of ice. This would enable us to match the performance of the WiSe
658 system (Smeets and others, 2012) but with more compact antennas, enabling the Cryoegg to ‘roam’
659 through englacial and subglacial hydrological systems to collect spatially and temporally distributed
660 measurements, reported in real time. Cryoegg technology will also be adapted for englacial studies in
661 irregular and refreezing hot-water-drilled boreholes, by creating a cylindrical form factor with a much
662 smaller diameter than Cryoegg, allowing deployment in a smaller borehole.

663 ACKNOWLEDGEMENTS

664 This work was funded by UK Engineering and Physical Sciences Research Council (EPSRC) New
665 Investigator Award EP/R03530X/1, awarded to Liz Bagshaw.

666 Thanks to all who assisted us in the field, in particular: Trevor Popp, Romain Duphil and the EastGRIP
667 drill team; “Mickey” MacKay, Eliza Dawson and Rob Law at the RESPONDER site; Lai Bun Lok, Jonathan
668 Hawkins, the ETH Zürich VAW Glaciology team and the Swiss Air Force at the Rhône Glacier site. Phil
669 Anderson gave us use of the RF test chamber. We are grateful for in-kind contributions of equipment
670 from Quadro and Radiocrafts. Particular thanks to the team at DGF Engineering for the machining of
671 the caseworks, to Protronix EMS Ltd for the rapid production of the electronics, and to Justin Johnson
672 of InnovAntennas for the custom design of the receiving antenna. Miles Gould provided assistance
673 with the algebra for Equation 3. We would particularly like to thank our anonymous reviewers for their
674 helpful contributions and suggestions.

675 EastGRIP is directed and organized by the Center of Ice and Climate at the Niels Bohr Institute. It is
676 supported by funding agencies and institutions in Denmark (A. P. Møller Foundation, University of
677 Copenhagen), USA (US National Science Foundation, Office of Polar Programs), Germany (Alfred
678 Wegener Institute, Helmholtz Centre for Polar and Marine Research), Japan (National Institute of Polar
679 Research and Arctic Challenge for Sustainability), Norway (University of Bergen and Bergen Research
680 Foundation), Switzerland (Swiss National Science Foundation), France (French Polar Institute Paul-
681 Emile Victor, Institute for Geosciences and Environmental research) and China (Chinese Academy of
682 Sciences and Beijing Normal University)

683 Bryn Hubbard acknowledges support for hot-water borehole drilling from HEFCW through a Capital
684 Equipment Grant awarded to Aberystwyth University, and from the NERC through grant NE/K006126.

685 The RESPONDER project is funded by a Consolidator Grant to Poul Christoffersen from the European
686 Research Council, under the European Union’s Horizon 2020 research and innovation programme
687 (Grant 683043).

688 Tom Chudley was supported by a Natural Environment Research Council Doctoral Training Partnership
689 Studentship (Grant NE/L002507/1).

690 ArcticDEM was created from DigitalGlobe, Inc., imagery and funded under National Science
691 Foundation awards 1043681, 1559691, and 1542736

693 REFERENCES

694

695 About LoRaWAN® | LoRa Alliance® <https://lora-alliance.org/about-lorawan>

696 Bagshaw EA, Burrow S, Wadham JL, Bowden J, Lishman B, Salter M, Barnes R and
697 Nienow P (2012) E-tracers: Development of a low cost wireless technique for
698 exploring sub-surface hydrological systems. *Hydrological Processes* **26**(20), 3157–
699 3160 (doi:10.1002/hyp.9451)

700 Bagshaw E, Karlsson NB, Lishman B, Lok LB, Burrow S, Wadham JL, Clare L, Nicholls
701 KW, Eisen O, Corr HFJ and Dahl-Jensen D (2018) Utilising Wireless Sensor
702 Technologies in Glaciology. *AGU Fall Meeting Abstracts* **43**
703 <http://adsabs.harvard.edu/abs/2018AGUFM.C43D1823B>

704 Bagshaw EA, Lishman B, Wadham JL, Bowden JA, Burrow SG, Clare LR and Chandler D
705 (2014) Novel wireless sensors for in situ measurement of sub-ice hydrologic systems.
706 *Annals of Glaciology* **55**(65), 41–50 (doi:10.3189/2014AoG65A007)

707 Barrella T, Barwick S and Saltzberg D (2011) Ross Ice Shelf in situ radio-frequency ice
708 attenuation. *Journal of Glaciology* **57**(201), 61–66
709 (doi:10.3189/002214311795306691)

710 Barwick S, Besson D, Gorham P and Saltzberg D (2005) South Polar in situ radio-frequency
711 ice attenuation. *Journal of Glaciology* **51**(173), 231–238
712 (doi:10.3189/172756505781829467)

713 van den Broeke MR, Enderlin EM, Howat IM, Kuipers Munneke P, Noël BPY, Berg WJ van
714 de, Meijgaard E van and Wouters B (2016) On the recent contribution of the
715 Greenland ice sheet to sea level change. *The Cryosphere* **10**(5), 1933–1946
716 (doi:<https://doi.org/10.5194/tc-10-1933-2016>)

717 Bullington K (1947) Radio Propagation at Frequencies above 30 Megacycles. *Proceedings of*
718 *the IRE* **35**(10), 1122–1136 (doi:10.1109/JRPROC.1947.232600)

719 Chandler DM, Wadham JL, Lis GP, Cowton T, Sole A, Bartholomew I, Telling J, Nienow P,
720 Bagshaw EB, Mair D, Vinen S and Hubbard A (2013) Evolution of the subglacial
721 drainage system beneath the Greenland Ice Sheet revealed by tracers. *Nature Geosci*
722 **6**(3), 195–198 (doi:10.1038/ngeo1737)

723 Chu VW (2014) Greenland ice sheet hydrology: A review. *Progress in Physical Geography:*
724 *Earth and Environment* **38**(1), 19–54 (doi:10.1177/0309133313507075)

725 Chudley TR, Christoffersen P, Doyle SH, Bougamont M, Schoonman CM, Hubbard B and
726 James MR (2019) Supraglacial lake drainage at a fast-flowing Greenlandic outlet
727 glacier. *PNAS* **116**(51), 25468–25477 (doi:10.1073/pnas.1913685116)

728 Church G, Bauder A, Grab M, Rabenstein L, Singh S and Maurer H (2019) Detecting and
729 characterising an englacial conduit network within a temperate Swiss glacier using
730 active seismic, ground penetrating radar and borehole analysis. *Annals of Glaciology*
731 **60**(79), 193–205 (doi:10.1017/aog.2019.19)

- 732 Clarke GKC (1987) Subglacial till: A physical framework for its properties and processes.
 733 *Journal of Geophysical Research: Solid Earth* **92**(B9), 9023–9036
 734 (doi:10.1029/JB092iB09p09023)
- 735 Dahl-Jensen D, Gundestrup N, Gogineni SP and Miller H (2003) Basal melt at NorthGRIP
 736 modeled from borehole, ice-core and radio-echo sounder observations. *Ann. Glaciol.*
 737 **37**, 207–212 (doi:10.3189/172756403781815492)
- 738 Davies K (1990) *Ionospheric Radio (IEE Electromagnetic Waves Series, Vol. 31)*. The
 739 Institution of Engineering and Technology
- 740 Doyle SH, Hubbard B, Christoffersen P, Young TJ, Hofstede C, Bougamont M, Box JE and
 741 Hubbard A (2018) Physical Conditions of Fast Glacier Flow: 1. Measurements From
 742 Boreholes Drilled to the Bed of Store Glacier, West Greenland. *Journal of*
 743 *Geophysical Research: Earth Surface* **123**(2), 324–348 (doi:10.1002/2017JF004529)
- 744 European Committee for Standardisation (2013) *BS EN 13757-4:2013 - Communication*
 745 *systems for meters and remote reading of meters . Wireless meter readout (Radio*
 746 *meter reading for operation in SRD bands)*. [https://bsol.bsigroup.com/en/Bsol-Item-](https://bsol.bsigroup.com/en/Bsol-Item-Detail-Page/?pid=000000000030249978)
 747 [Detail-Page/?pid=000000000030249978](https://bsol.bsigroup.com/en/Bsol-Item-Detail-Page/?pid=000000000030249978)
- 748 Flowers GE (2018) Hydrology and the future of the Greenland Ice Sheet. *Nature*
 749 *Communications* **9**(1), 2729 (doi:10.1038/s41467-018-05002-0)
- 750 Friis HT (1946) A Note on a Simple Transmission Formula. *Proceedings of the IRE* **34**(5),
 751 254–256 (doi:10.1109/JRPROC.1946.234568)
- 752 Griffiths J (1987) *Radio wave propagation and antennas*. Prentice-Hall
- 753 Gulley J (2009) Structural control of englacial conduits in the temperate Matanuska Glacier,
 754 Alaska, USA. *Journal of Glaciology* **55**(192), 681–690
 755 (doi:10.3189/002214309789470860)
- 756 Gundrestrup NS, Clausen HB and Hansen BL (1994) The UCPH borehole logger. *Memoirs*
 757 *of National Institute of Polar Research Special Issue* **49**, 224–233
 758 <https://icedrill.org/library/ucph-borehole-logger>
- 759 Hargreaves ND (1978) The Radio-Frequency Birefringence of Polar Ice. *Journal of*
 760 *Glaciology* **21**(85), 301–313 (doi:10.3189/S0022143000033499)
- 761 Hart JK, Martinez K, Basford PJ, Clayton AI, Robson BA and Young DS (2019) Surface
 762 melt driven summer diurnal and winter multi-day stick-slip motion and till
 763 sedimentology. *Nat Commun* **10**(1), 1–11 (doi:10.1038/s41467-019-09547-6)
- 764 Hoffman MJ, Andrews LC, Price SF, Catania GA, Neumann TA, Lüthi MP, Gulley J, Ryser
 765 C, Hawley RL and Morriss B (2016) Greenland subglacial drainage evolution
 766 regulated by weakly connected regions of the bed. *Nat Commun* **7**(1), 1–12
 767 (doi:10.1038/ncomms13903)
- 768 Hofstede C, Christoffersen P, Hubbard B, Doyle SH, Young TJ, Diez A, Eisen O and
 769 Hubbard A (2018) Physical Conditions of Fast Glacier Flow: 2. Variable Extent of
 770 Anisotropic Ice and Soft Basal Sediment From Seismic Reflection Data Acquired on

- 771 Store Glacier, West Greenland. *Journal of Geophysical Research: Earth Surface*
772 **123**(2), 349–362 (doi:10.1002/2017JF004297)
- 773 Holmlund P and Hooke RLeb (1983) High Water-Pressure Events in Moulins, Storglaciären,
774 Sweden. *Geografiska Annaler: Series A, Physical Geography* **65**(1–2), 19–25
775 (doi:10.1080/04353676.1983.11880070)
- 776 Hubbard BP, Sharp MJ, Willis IC, Nielsen MK and Smart CC (1995) Borehole water-level
777 variations and the structure of the subglacial hydrological system of Haut Glacier
778 d’Arolla, Valais, Switzerland. *Journal of Glaciology* **41**(139), 572–583
779 (doi:10.3189/S0022143000034894)
- 780 Iken A (1972) Measurements of Water Pressure in Moulins as Part of a Movement Study of
781 the White Glacier, Axel Heiberg Island, Northwest Territories, Canada. *Journal of*
782 *Glaciology* **11**(61), 53–58 (doi:10.3189/S0022143000022486)
- 783 Iken A (1981) The Effect of the Subglacial Water Pressure on the Sliding Velocity of a
784 Glacier in an Idealized Numerical Model. *Journal of Glaciology* **27**(97), 407–421
785 (doi:10.3189/S0022143000011448)
- 786 Iken A and Bindschadler RA (1986) Combined measurements of Subglacial Water Pressure
787 and Surface Velocity of Findelengletscher, Switzerland: Conclusions about Drainage
788 System and Sliding Mechanism. *Journal of Glaciology* **32**(110), 101–119
789 (doi:10.3189/S0022143000006936)
- 790 Iken A, Echelmeyer K, Harrison W and Funk M (1993) Mechanisms of fast flow in
791 Jakobshavns Isbræ, West Greenland: Part I. Measurements of temperature and water
792 level in deep boreholes. *Journal of Glaciology* **39**(131), 15–25
793 (doi:10.3189/S0022143000015689)
- 794 Joughin I (2017) MEaSURES Greenland Ice Velocity Annual Mosaics from SAR and
795 Landsat, Version 1. (doi:10.5067/OBXCG75U7540)
- 796 Joughin I, Smith BE, Howat IM, Scambos T and Moon T (2010) Greenland flow variability
797 from ice-sheet-wide velocity mapping. *Journal of Glaciology* **56**(197), 415–430
798 (doi:10.3189/002214310792447734)
- 799 Kamb B (1970) Sliding motion of glaciers: Theory and observation. *Reviews of Geophysics*
800 **8**(4), 673–728 (doi:10.1029/RG008i004p00673)
- 801 Kamb B (1987) Glacier surge mechanism based on linked cavity configuration of the basal
802 water conduit system. *Journal of Geophysical Research: Solid Earth* **92**(B9), 9083–
803 9100 (doi:10.1029/JB092iB09p09083)
- 804 Karlsson NB and Dahl-Jensen D (2015) Response of the large-scale subglacial drainage
805 system of Northeast Greenland to surface elevation changes. *The Cryosphere* **9**(4),
806 1465–1479 (doi:https://doi.org/10.5194/tc-9-1465-2015)
- 807 Lewis C, Gogineni S, Rodriguez-Morales F, Panzer B, Stumpf T, Paden J and Leuschen C
808 (2015) Airborne fine-resolution UHF radar: an approach to the study of englacial
809 reflections, firn compaction and ice attenuation rates. *J. Glaciol.* **61**(225), 89–100
810 (doi:10.3189/2015JoG14J089)

- 811 Li J, Vélez González JA, Leuschen C, Harish A, Gogineni P, Montagnat M, Weikusat I,
812 Rodríguez-Morales F and Paden J (2018) Multi-channel and multi-polarization radar
813 measurements around the NEEM site. *The Cryosphere* **12**(8), 2689–2705
814 (doi:<https://doi.org/10.5194/tc-12-2689-2018>)
- 815 MacGregor JA, Li J, Paden JD, Catania GA, Clow GD, Fahnestock MA, Gogineni SP,
816 Grimm RE, Morlighem M, Nandi S, Seroussi H and Stillman DE (2015) Radar
817 attenuation and temperature within the Greenland Ice Sheet. *Journal of Geophysical*
818 *Research: Earth Surface* **120**(6), 983–1008 (doi:10.1002/2014JF003418)
- 819 MacGregor JA, Winebrenner DP, Conway H, Matsuoka K, Mayewski PA and Clow GD
820 (2007) Modeling englacial radar attenuation at Siple Dome, West Antarctica, using
821 ice chemistry and temperature data. *Journal of Geophysical Research: Earth Surface*
822 **112**(F3) (doi:10.1029/2006JF000717)
- 823 Martinez K, Basford PJ, Jager DD and Hart JK (2013) Using a heterogeneous sensor network
824 to monitor glacial movement. 2
- 825 Martinez K, Ong R and Hart J (2004) Glacsweb: a sensor network for hostile environments.
826 *2004 First Annual IEEE Communications Society Conference on Sensor and Ad Hoc*
827 *Communications and Networks, 2004. IEEE SECON 2004.* 81–87
828 (doi:10.1109/SAHCN.2004.1381905)
- 829 Moore RD (2005) Introduction to salt dilution gauging for streamflow measurement Part 3:
830 Slug injection using salt in solution. *Streamline Watershed Management Bulletin* **8**(2),
831 1–6
- 832 Morlighem M, Williams CN, Rignot E, An L, Arndt JE, Bamber JL, Catania G, Chauché N,
833 Dowdeswell JA, Dorschel B, Fenty I, Hogan K, Howat I, Hubbard A, Jakobsson M,
834 Jordan TM, Kjeldsen KK, Millan R, Mayer L, Mouginot J, Noël BPY, O’Cofaigh C,
835 Palmer S, Rysgaard S, Seroussi H, Siegert MJ, Slabon P, Straneo F, van den Broeke
836 MR, Weinrebe W, Wood M and Zinglensen KB (2017) BedMachine v3: Complete
837 Bed Topography and Ocean Bathymetry Mapping of Greenland From Multibeam
838 Echo Sounding Combined With Mass Conservation. *Geophysical Research Letters*
839 **44**(21), 11,051–11,061 (doi:10.1002/2017GL074954)
- 840 Ng FSL (2000) Canals under sediment-based ice sheets. *Annals of Glaciology* **30**, 146–152
841 (doi:10.3189/172756400781820633)
- 842 Nienow PW, Hubbard AL, Hubbard BP, Chandler DM, Mair DWF, Sharp MJ and Willis IC
843 (2005) Hydrological controls on diurnal ice flow variability in valley glaciers. *Journal*
844 *of Geophysical Research: Earth Surface* **110**(F4) (doi:10.1029/2003JF000112)
- 845 Nienow PW, Sole AJ, Slater DA and Cowton TR (2017) Recent Advances in Our
846 Understanding of the Role of Meltwater in the Greenland Ice Sheet System. *Curr*
847 *Clim Change Rep* **3**(4), 330–344 (doi:10.1007/s40641-017-0083-9)
- 848 Nye JF (1976) Water Flow in Glaciers: Jökulhlaups, Tunnels and Veins. *Journal of*
849 *Glaciology* **17**(76), 181–207 (doi:10.3189/S002214300001354X)
- 850 Plewes LA and Hubbard B (2001) A review of the use of radio-echo sounding in glaciology:
851 *Progress in Physical Geography* (doi:10.1177/030913330102500203)

- 852 Porter C, Morin P, Howat I, Noh M-J, Bates B, Peterman K, Keeseey S, Schlenk M, Gardiner
853 J, Tomko K, Willis M, Kelleher C, Cloutier M, Husby E, Foga S, Nakamura H,
854 Platson M, Wethington M Jr, Williamson C, Bauer G, Enos J, Arnold G, Kramer W,
855 Becker P, Doshi A, D'Souza C, Cummens P, Laurier F and Bojesen M (2018)
856 ArcticDEM. (doi:10.7910/DVN/OHHUKH)
- 857 Pritchard HD, Arthern RJ, Vaughan DG and Edwards LA (2009) Extensive dynamic thinning
858 on the margins of the Greenland and Antarctic ice sheets. *Nature* **461**(7266), 971–975
859 (doi:10.1038/nature08471)
- 860 RC1701xx-MBUS Datasheet (2018) [https://radiocrafts.com/uploads/rc1701xx-
mbus_datasheet.pdf](https://radiocrafts.com/uploads/rc1701xx-
861 mbus_datasheet.pdf)
- 862 Röthlisberger H (1972) Water Pressure in Intra- and Subglacial Channels *. *Journal of*
863 *Glaciology* **11**(62), 177–203 (doi:10.3189/S0022143000022188)
- 864 Röthlisberger H (1980) Gletscherbewegung und Wasserabfluss. *Wasser, Energie, Luft* **72**(9),
865 290–294
- 866 Röthlisberger H and Lang H (1987) Glacial Hydrology. *Glacio-Fluvial Sediment Transfer:*
867 *An Alpine Perspective*. Wiley, 207–84
- 868 Schoof C (2010) Ice-sheet acceleration driven by melt supply variability. *Nature* **468**(7325),
869 803–806 (doi:10.1038/nature09618)
- 870 Sheldon SG, Steffensen JP, Hansen SB, Popp TJ and Johnsen SJ (2014) The investigation
871 and experience of using ESTISOL™ 240 and COASOL™ for ice-core drilling.
872 *Annals of Glaciology* **55**(68), 219–232 (doi:10.3189/2014AoG68A036)
- 873 Smeets CJPP, Boot W, Hubbard A, Pettersson R, Wilhelms F, Broeke MRVD and Wal
874 RSWVD (2012) A wireless subglacial probe for deep ice applications. *Journal of*
875 *Glaciology* **58**(211), 841–848 (doi:10.3189/2012JoG11J130)
- 876 Sole AJ, Mair DWF, Nienow PW, Bartholomew ID, King MA, Burke MJ and Joughin I
877 (2011) Seasonal speedup of a Greenland marine-terminating outlet glacier forced by
878 surface melt-induced changes in subglacial hydrology. *Journal of Geophysical*
879 *Research: Earth Surface* **116**(F3) (doi:10.1029/2010JF001948)
- 880 Stott J (2005) BBC R&D White Paper WHP 109: Digital Radio Mondiale: DRM, digital
881 radio on long, medium and short waves – another radio revolution?
882 <http://downloads.bbc.co.uk/rd/pubs/whp/whp-pdf-files/WHP109.pdf>
- 883 Tedstone AJ, Nienow PW, Gourmelen N, Dehecq A, Goldberg D and Hanna E (2015)
884 Decadal slowdown of a land-terminating sector of the Greenland Ice Sheet despite
885 warming. *Nature* **526**(7575), 692–695 (doi:10.1038/nature15722)
- 886 Tranter M, Sharp MJ, Lamb HR, Brown GH, Hubbard BP and Willis IC (2002) Geochemical
887 weathering at the bed of Haut Glacier d’Arolla, Switzerland—a new model.
888 *Hydrological Processes* **16**(5), 959–993 (doi:10.1002/hyp.309)
- 889 UM10204 I2C-bus specification and user manual (2014) **2014**, 64

- 890 Walder JS (1986) Hydraulics of Subglacial Cavities. *Journal of Glaciology* **32**(112), 439–445
891 (doi:10.3189/S0022143000012156)
- 892 Werder MA, Schuler TV and Funk M (2010) Short term variations of tracer transit speed on
893 alpine glaciers. *The Cryosphere* **4**(3), 381–396 (doi:[https://doi.org/10.5194/tc-4-381-](https://doi.org/10.5194/tc-4-381-2010)
894 2010)
- 895 Young TJ, Schroeder DM, Christoffersen P, Lok LB, Nicholls KW, Brennan PV, Doyle SH,
896 Hubbard B and Hubbard A (2018) Resolving the internal and basal geometry of ice
897 masses using imaging phase-sensitive radar. *Journal of Glaciology* **64**(246), 649–660
898 (doi:10.1017/jog.2018.54)
- 899
- 900

SUPPLEMENTARY MATERIAL

Activity	Quantity	Unit
Energy consumption during measure and transmit	0.5	J
Duration of measure and transmit	3.2	s
Current consumption during sleep	500	nA
Nominal battery voltage	3.7	V
Power consumption during sleep	1.85	uW
Battery nominal voltage	3.7	V
Battery nominal capacity	400	mAh
Battery nominal capacity	1.48	Wh
Battery nominal capacity	5328	J
Derate factor for operating in the cold	50%	
Battery effective capacity in the field	2664	J
For 2 measurements per day:		
Active measurement time per day:	6.4	seconds
Sleep time per day	86393.6	seconds
Energy used whilst active	1	J
Energy used whilst asleep	0.16	J
Total energy used per day	1.16	J
Number of days the system will run for	2296	days
Number of years the system will run for	6.3	years

Table S1 – battery life calculation